Chemical Engineering Journal Advances 27 (2026) 101296

Contents lists available at ScienceDirect

Chemical Engineering Journal Advances

journal homepage: www.sciencedirect.com/journal/chemical-engineering-journal-advances

iTransKAN: A deep chemometric model for enhanced heavy metal quantification via multi-scan cyclic voltammetry

Fadlilatul Taufany [a], Rizqy Ahsana Putri [b], Riyanarto Sarno [b,*], Wahyu Prasetyo Utomo [c], Kelly Rossa Sungkono [b], Arif Abdullah Sagran [d]

[a] Department of Chemical Engineering, Institut Teknologi Sepuluh Nopember, Surabaya, 60111, Indonesia
[b] Department of Informatics, Institut Teknologi Sepuluh Nopember, Surabaya, 60111, Indonesia
[c] Department of Chemistry, Institut Teknologi Sepuluh Nopember, Surabaya, 60111, Indonesia
[d] Faculdade de Ciências Políticas, Universidade Dili, Dili, 66000, Timor-Leste

ARTICLE INFO

Dataset link: https://github.com/ahsnputri/iTransKAN

Keywords:
Chemometric
iTransKAN
Learnable positional encoding
Multi-scan cyclic voltammetry
Relative asymmetric toxicity error
Scan-level attention fusion
Water pollution

ABSTRACT

Voltammetric analysis coupled with advanced chemometrics provides a powerful framework for heavy metal quantification. However, translating complex, non-linear electrical current responses into precise concentrations remains challenging. Conventional models and standard Transformers struggle with the quadratic computational burden of sequential data and are limited in their ability to fully capture progressive signal variations across multi-scan operations. Furthermore, standard symmetric evaluation metrics assign equal penalties to all errors and critically ignore the severe environmental hazards of toxicity underestimations. To overcome these limitations, this study proposes iTransKAN, a deep chemometric framework integrating an Inverted Transformer for efficient global feature extraction with a Kolmogorov–Arnold Network (KAN) for highly flexible regression. The architecture is further refined by a Learnable Positional Encoding to capture complex sequential shifts in the voltammetric data, alongside a Scan-Level Attention Fusion to effectively aggregate informative signal patterns across scanning cycles. A novel Relative Asymmetric Toxicity Error (RATE) metric is also introduced to penalize hazardous under-predictions while maintaining evaluation fairness. Experimental results and Wilcoxon signed-rank tests confirm that iTransKAN significantly outperforms the standard iTransformer baseline ($p < 0.001$). This integration reduces the Mean Absolute Error (MAE) by 72.2% for Pb and 33.8% for Cd. Consequently, the proposed model achieves a robust R^2 of 0.9997 (95% CI: 0.9993–1.0000) for Pb and 0.9814 (95% CI: 0.9570–1.0000) for Cd. These findings highlight the potential of iTransKAN to provide highly accurate, computationally efficient, and safety-aware heavy metal quantification for advanced environmental sensing.

1. Introduction

Chemometrics provides the essential mathematical and statistical framework required to extract meaningful chemical information from instrumental data [1,2]. Within voltammetric analysis, chemometrics is crucial to translate complex electrical current responses into precise heavy metal concentrations [3]. Early chemometric practices relied heavily on univariate calibration and traditional multivariate methods, such as Principal Component Regression (PCR) and Partial Least Squares (PLS) [4–6]. These traditional methods offer high interpretability and computational simplicity, but standard linear models operate under strict linearity assumptions [7,8]. Consequently, these methods face fundamental limitations when processing real-world measurement signals that exhibit highly fluctuating characteristics and complex non-linear patterns.

Researchers have adopted Machine Learning (ML) algorithms to overcome the constraints of traditional linear models [9,10]. Algorithms such as Support Vector Machines (SVM) and Random Forests demonstrate superior capability in mapping non-linear chemical relationships during heavy metal detection tasks [9,10]. However, conventional machine learning frameworks inherently demand labor-intensive manual feature extraction to achieve optimal analytical accuracy. Deep Learning (DL) architectures subsequently emerged as a powerful computational alternative to completely eliminate the manual feature extraction phase [11]. Numerous recent studies regarding heavy metal prediction actively deploy advanced DL architectures including Convolutional Neural Networks (CNN) [12] and Artificial Neural Networks (ANN) [13,14]. However, typical neural networks introduce distinct

* Corresponding author.
E-mail address: riyanarto@its.ac.id (R. Sarno).

https://doi.org/10.1016/j.ceja.2026.101296
Received 27 March 2026; Received in revised form 1 June 2026; Accepted 8 June 2026
Available online 12 June 2026

structural disadvantages. Standard architectures utilize rigid activation functions and lack specialized mechanisms to efficiently process the inherently sequential nature of voltammetric data [15]. The architectural limitations of standard neural networks necessitate a shift toward advanced sequence-modeling frameworks capable of capturing data dependencies directly from raw time-series measurements.

Sequence-modeling frameworks have significantly advanced following the introduction of the Transformer architecture [16]. The Transformer relies on self-attention mechanisms to process sequential data effectively [17]. However, the direct application of standard Transformers to voltammetric analysis presents severe computational challenges. Continuous voltammetric sweeps inherently generate highly extended high-density measurement sequences. Standard attention mechanisms explicitly compute feature correlations across every individual time step. The strictly correlation process consequently generates a massive quadratic computational burden [18]. Additionally, the strict time-step focus forces the network to prioritize minor signal variations rather than capturing the global morphological features of the data.

Recent advancements in deep learning introduced the Inverted Transformer (iTransformer) architecture to resolve the computational inefficiencies of standard Transformer [19]. The inverted architecture fundamentally reverses the conventional self-attention logic [20]. Instead of calculating attention across individual time steps, the iTransformer embeds the entire sequence as a single token and computes correlations globally across feature dimensions with minimal computational complexity [19,21,22]. The inverted structure also allows the network to extract comprehensive representations of the voltammetric sequence without interference from minor time-step fluctuations.

Because the core self-attention operation lacks inherent sequential awareness, Transformer-based architectures fundamentally rely on Positional Encoding (PE) mechanisms to identify the sequential order of input data [23,24]. Standard PE mechanisms utilize static mathematical formulas, specifically sine and cosine functions [25,26]. These static formulas, however, are rigid and lack the adaptability to respond to irregular signal variations that occur across sequential scans. Accurate sequence order recognition remains highly crucial because voltammetric experiments often employ sequential multi-scan methods to gather comprehensive measurement data [27,28]. While continuous scanning cycles are known to induce complex variations on the sensor surface over time [29], these phenomena inherently manifest as non-linear, progressive shifts in the recorded data. Consequently, standard static PE exhibit limitations in fully capturing these complex sequential data patterns, which can constrain the overall representational accuracy of the model.

Synthesizing data from multiple scanning cycles introduces another critical data aggregation challenge. Conventional aggregation approaches typically employ average pooling to merge multiple scan curves into a single output [30]. Average pooling assigns equal importance to all measurements. The equal-weighting approach fails to recognize the varying informational value across different scanning cycles. Assigning uniform weights prevents the network from dynamically prioritizing specific scans that provide the most critical features for accurate prediction [31].

Advanced feature extraction models such as the iTransformer remain insufficient for complete voltammetric quantification. A subsequent regression network must map the synthesized features into accurate concentration values. Conventional frameworks typically employ a standard Multi-Layer Perceptron (MLP) as the regression head [32,33]. Standard MLPs encounter profound limitations in chemical sensor applications because the relationship between the measured signal and the actual concentration frequently becomes highly non-linear [34,35]. The Kolmogorov–Arnold Network (KAN) emerged as a highly effective alternative to standard regression networks. The KAN framework replaces rigid activation functions with learnable spline-based functions on the network edges [36]. The flexible spline functions allow the model to continuously adapt and map extreme non-linear relationships with exceptional accuracy.

Validating the exceptional accuracy of advanced regression networks intrinsically requires an appropriate evaluation metric. Conventional analytical studies predominantly utilize standard error measurements, specifically Root Mean Square Error (RMSE) [37,38] and Mean Absolute Error (MAE) [39]. Standard error metrics inherently calculate prediction deviations symmetrically. Symmetric calculations assign identical mathematical penalties to both over-estimated predictions and under-estimated predictions. However, under-estimations within critical applications such as toxic heavy metal prediction pose exceptionally severe environmental and public health hazards compared to over-estimations.

A comprehensive review of the preceding literature reveals four critical limitations within current deep chemometric frameworks: (1) conventional regression networks lack the structural flexibility required to generate accurate predictions for heavy metal targets from complex voltammetric data; (2) static positional formulas process measurement sequences rigidly and exhibit limitations in capturing the progressive signal variations induced by continuous multi-scan operations; (3) uniform aggregation methods merge all measurement iterations indiscriminately and obscure highly informative signal patterns; and (4) standard evaluation criteria treat directional errors equally and ignore the practical dangers of toxicity underestimations. To address these gaps, this research proposes the following contributions:

1. We propose iTransKAN, a novel deep chemometric framework combining iTransformer feature extraction with KAN regression to accurately model severe calibration non-linearities over a wide dynamic range of heavy metal concentrations.
2. We propose a Learnable PE mechanism that effectively captures the temporal order of the sequential scanning cycles to dynamically learn and adapt to progressive signal variations without relying on fixed mathematical functions.
3. We develop a Scan-Level Attention Fusion mechanism that dynamically assigns proportional attention weights to each scan to synthesize a reliable final representation.
4. We propose the Relative Asymmetric Toxicity Error (RATE) metric, a novel evaluation function that heavily penalizes potentially hazardous under-predictions while maintaining relative fairness across trace and high concentration levels.

The remaining sections of the article are organized as follows. Section 2 elaborates on the architectural design of the proposed methodology. Section 3 discusses the performance evaluations and experimental findings. Finally, Section 4 delivers the concluding remarks and suggests directions for future investigations.

2. Proposed method

The current section details the proposed deep chemometric framework designed for precise heavy metal quantification from complex voltammetric data. As illustrated in Fig. 1, the complete methodology encompasses seven distinct sequential stages: (1) data acquisition; (2) feature engineering; (3) data preprocessing; (4) data splitting; (5) design of the proposed iTransKAN framework; (6) dynamic network refinements via learnable sequence encoding and scan-level fusion; and (7) comprehensive performance evaluation utilizing the asymmetric RATE metric.

2.1. Data acquisition

Voltammetric analysis fundamentally quantifies analyte concentrations by measuring the generated electrical current in response to an applied potential range [40]. The current study utilizes Cyclic Voltammetry (CV) to observe the intricate reduction and oxidation behaviors

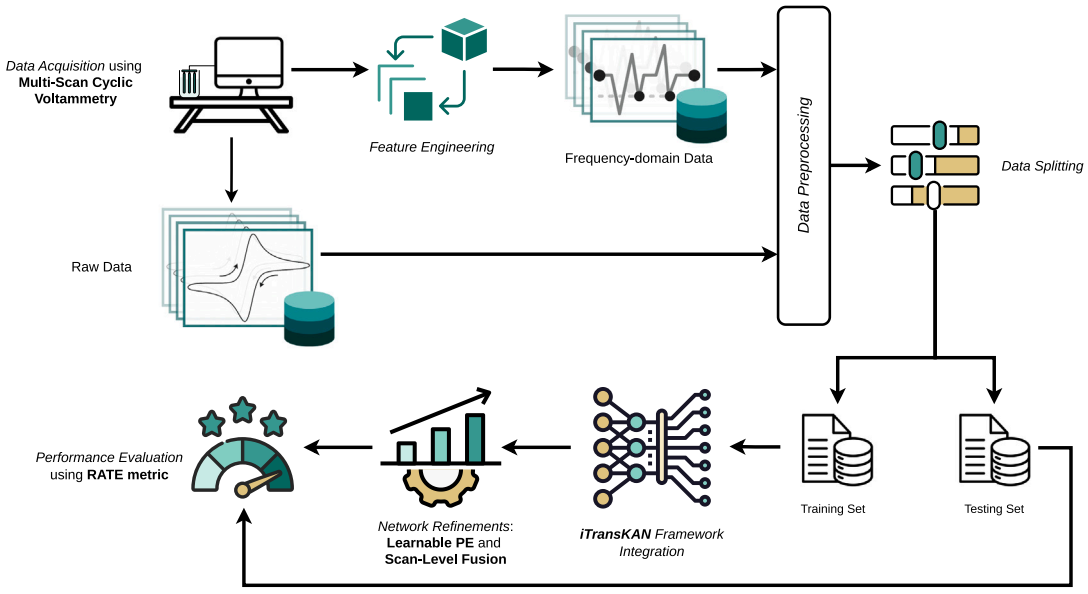

Fig. 1. The proposed method.

of the target heavy metals [41]. Standard CV operations typically employ a single voltage sweep [42,43]. However, the proposed methodology implements a multi-scan CV approach consisting of 10 continuous consecutive cycles. Continuous multi-scan operations are highly crucial to accurately capture the progressive chemical kinetic variations and dynamic surface degradation patterns occurring on the sensor interface over time. The measurement system employs a high-precision PalmSens4 potentiostat driven by PSTrace software [44]. The PalmSens4 instrument maintains absolute voltage control across a standard three-electrode electrochemical cell. The specific cell configuration includes a Glassy Carbon Electrode (GCE) serving as the working electrode, a Platinum wire acting as the counter electrode, and an Ag/AgCl (3M KCl) reference electrode [45].

Accurate voltammetric detection intrinsically requires an uncontaminated working electrode surface. The experimental protocol mandates a rigorous physical and chemical cleaning procedure for the GCE prior to every single measurement sequence. The cleaning process involves sequential immersion of the electrode tip into acidic and alkaline solutions to dissolve accumulated organic and inorganic impurities. Subsequent rinsing with deionized water eliminates all residual cleaning agents from the carbon surface. The procedure concludes by gently drying the electrode surface using chemical wipes to prevent microscopic physical abrasions.

The experimental phase evaluated the electrochemical responses of Cadmium (Cd) and Lead (Pb) targets at ambient room temperature. These specific heavy metals were selected as target analytes because they are highly toxic [46], frequently co-occur in industrial effluents [47], and serve as a rigorous analytical benchmark for environmental monitoring [48,49]. The analytical preparation involved formulating standard solutions across 15 discrete concentration levels categorized into three progressive measurement scales. The calibration scheme included a low-concentration range from 2 to 10 ppm with 2 ppm increments, a medium-concentration range from 20 to 100 ppm with 20 ppm increments, and a high-concentration range from 200 to 1000 ppm with 200 ppm increments. To construct a robust and sufficiently large dataset for deep learning, each of the 15 concentration levels underwent 50 independent measurement repetitions per analyte. This rigorous acquisition protocol yielded a comprehensive total of 1500 voltammetric samples. The standard solutions utilized high-purity $Cd(NO_3)_2$ and $Pb(NO_3)_2$ compounds dissolved in a 0.1 M KCl supporting electrolyte. During the measurement execution, exactly 20 mL of the prepared solution was transferred into the electrochemical cell. The PalmSens4 potentiostat scanned the applied voltage at a constant scan rate of 0.1 V/s. For the Cd samples, the voltage sweep ranged from −1.4 V to −0.5 V. Conversely, the voltage sweep for the Lead samples ranged from −1.0 V to −0.1 V.

The PSTrace software automatically records the dynamic electrochemical responses and exports the raw measurements into standardized spreadsheet formats. The exported dataset comprises exact voltage–current coordinate pairs mapped individually for all 10 scanning cycles.

2.2. Feature engineering

Feature engineering is a fundamental data transformation process in machine learning, designed to derive highly representative structural metrics from continuous measurement signals. While discrete morphological peak parameters have been utilized in previous automated extraction protocols [39], this study formally transitions to frequency-domain features to more comprehensively capture dynamic signal variations. A Fast Fourier Transform (FFT) algorithm was applied to the voltammetric sequences to capture the spectral amplitude distribution and identify the principal frequency components [50].

Ultimately, this feature engineering stage generates a structured alternative dataset composed of discrete spectral features. As a result, two distinct data representations are exclusively employed and comparatively analyzed in this research: (1) raw data (continuous signals without feature engineering) and (2) frequency-domain data. Each data instance across both representations encompasses 10 consecutive voltammetric scans.

2.3. Data preprocessing

The objective of data preprocessing is to condition the raw measurements and extracted features prior to computational network training. Rigorous preprocessing algorithms ensure optimal numerical stability and effectively accelerate the convergence rate of complex regression

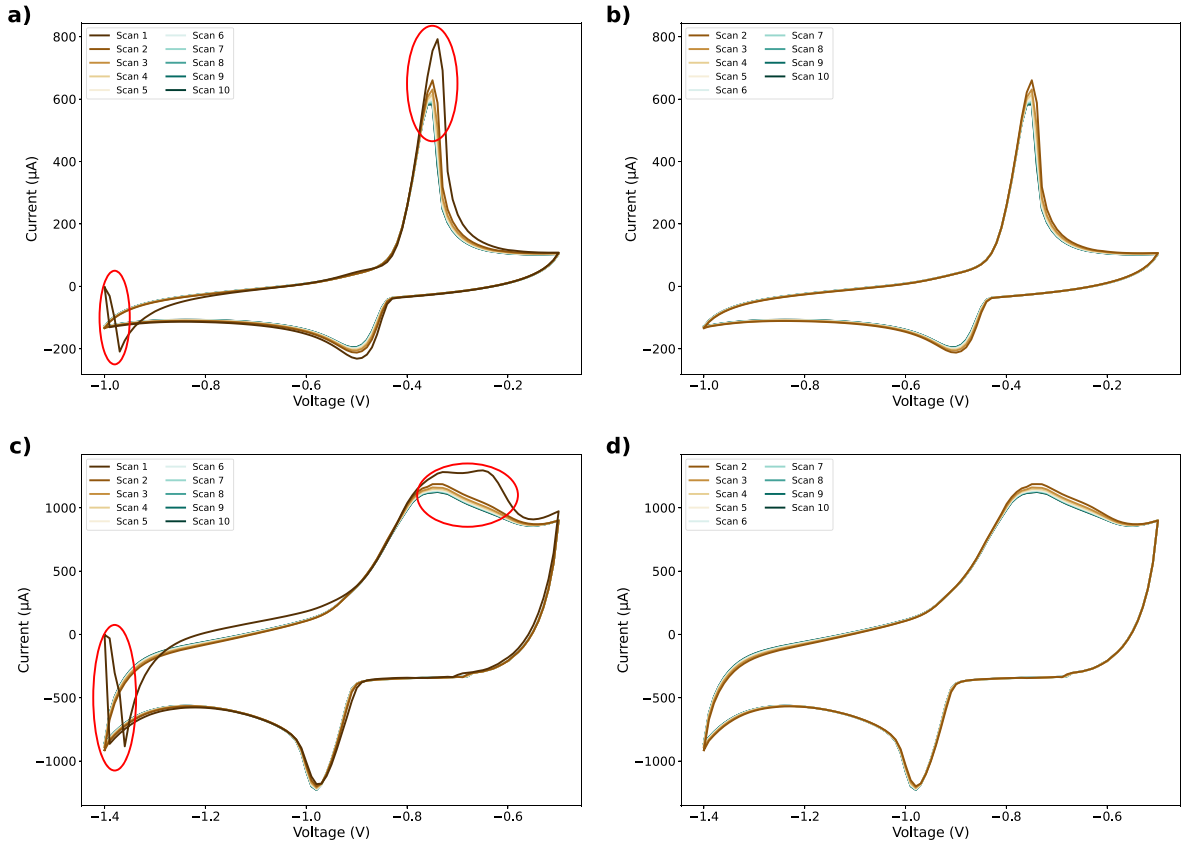

Fig. 2. Multi-scan CV data illustrating the stabilization phase during Pb (a, b) and Cd (c, d) detection. The left panels (a, c) display the complete sequence of 10 consecutive scans, with red ellipses highlighting the pronounced anomalies specific to Scan 1. The right panels (b, d) present the stabilized current responses (Scans 2–10) following the removal of the initial scan during the preprocessing step.

models [51]. This study implements three critical preprocessing mechanisms across both the raw data and the frequency-domain data. The most crucial initial procedure permanently discards the first voltammetric cycle (Scan 1) from every measurement sequence. Initial scans consistently exhibit highly unstable background currents and distinct morphological deviations, particularly at the starting edges of the voltage sweep. Fig. 2 explicitly illustrates the severe geometric discrepancies between the anomalous Scan 1 and the stabilized subsequent scans. Beyond these visual deviations, a quantitative assessment confirms this instability. For the Pb measurements, the average current of Scan 1 is an extreme outlier at −4.2326 μA, whereas the averages for the subsequent scans (Scans 2–9) stabilize between −8.2113 μA and −6.7230 μA. Similarly, for the Cd target, the Scan 1 average is isolated at −16.3655 μA, while the remaining scans settle into a stable range of −63.0753 μA to −58.4048 μA. Because this initial scan primarily reflects the physical sensor equilibration rather than useful transient information, eliminating it effectively prevents computational instability during the deep learning phase. Subsequently, the data are normalized using a Standard Scaler, computed according to Eq. (1) [52]. This step serves to standardize the data range across all features [53,54].

$$z = \frac{x - \mu}{\sigma} \tag{1}$$

where z represents the standardized output value, x denotes the original measurement point, μ signifies the empirical mean of the training distribution, and σ indicates the corresponding standard deviation.

The final preparation step applies a zero-padding technique exclusively to the continuous raw voltammograms. Instrumental recordings occasionally produce slight temporal variations regarding the total number of recorded data points per scan. Zero-padding strictly equalizes the absolute sequence lengths by appending zeros to the shorter temporal arrays [55]. Uniform sequence dimensions are absolutely mandatory to satisfy the rigid input matrix requirements of the proposed neural network architecture.

2.4. Data splitting

Data splitting represents a fundamental validation mechanism within computational modeling pipelines, establishing an independent evaluation for predictive networks. To ensure objective performance assessments on truly unseen data, the partitioning is strictly executed at the experimental run level. This protocol guarantees that the physical liquid samples and measurement beakers utilized in the testing set are completely distinct from those in the training set, thereby absolutely preventing any data leakage.

This study implements a 5-fold cross-validation strategy [56], which systematically mitigates critical methodological risks regarding algorithmic overfitting and unsubstantiated performance overclaims. The five-fold distribution algorithm mandates a strict 80:20 partitioning ratio during every validation iteration. Consequently, each fold allocates precisely 1200 isolated samples toward the neural network training phase, while the remaining 300 independent samples function strictly as the sequestered testing set.

2.5. The proposed iTransKAN architecture

Deep learning architectures represent a primary approach for predictive modeling in complex multivariate analysis. The proposed framework introduces a hybrid neural network designated as iTransKAN. This novel architecture synergistically integrates the inverted multivariate sequence-modeling capabilities of the iTransformer with the superior

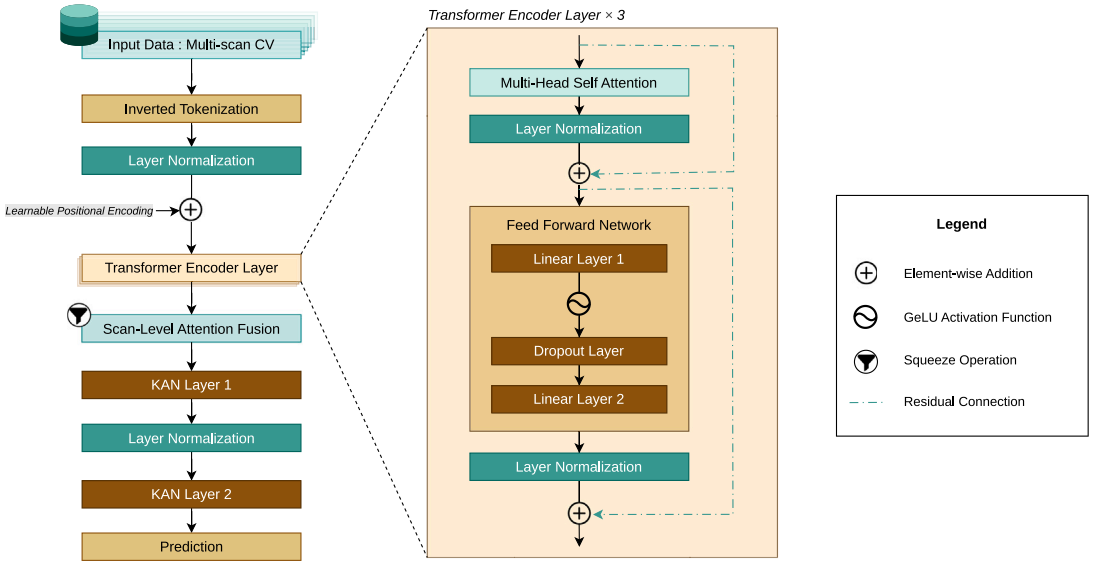

Fig. 3. The complete architecture of the proposed iTransKAN model.

non-linear mapping proficiency of KAN. Fig. 3 illustrates the complete workflow of the model.

The iTransformer represents a profound paradigm shift in modern sequence modeling. Standard transformer models typically tokenize temporal variations of individual variables across a designated sequence length. The iTransformer fundamentally reverses the tokenization dimension [20]. The inverted network embeds the entire temporal sequence of a single multivariate feature into one unified sequence token [21]. Similarly, the KAN provides a revolutionary mathematical alternative to traditional MLP. The KAN architecture completely abandons fixed activation functions located on fixed nodes. KAN deploys dynamically learnable activation functions directly upon the connective network edges [36].

The computational process of iTransKAN starts with an input matrix containing nine discrete consecutive voltammetric scans. Through an inverted tokenization mechanism, an initial linear projection maps the multi-scan CV data into a predefined latent space. A layer normalization process subsequently stabilizes the resulting data distribution. The complete mathematical tokenization process operates according to Eq. (2) [57,58].

$$H_{token} = \text{LayerNorm}(X \cdot W_{proj} + b_{proj}) \tag{2}$$

where H_{token} represents the normalized latent token representation, X denotes the input voltammetric scan matrix, W_{proj} indicates the learnable linear projection weight matrix, and b_{proj} signifies the projection bias vector.

The model requires sequence order awareness before executing the self-attention mechanism. A learnable PE vector is therefore added to the latent token. The mathematical formulation and specific details of this learnable PE are explained comprehensively in the subsequent subsection. The encoded representations subsequently proceed into three consecutive Transformer Encoder layers. Each layer consists of a Multi-Head Self-Attention (MHSA) module and a Feed-Forward Network (FFN) [59]. The network architecture specifically positions a layer normalization step after the MHSA computation and subsequently adds the original input via a residual connection. The MHSA module extracts inter-scan relationships according to Eq. (3) [57].

$$H_{attn} = \text{LayerNorm}(\text{MHSA}(H_{in})) \oplus H_{in} \tag{3}$$

where H_{attn} is the intermediate attention output, MHSA represents the multi-head self-attention operation, and H_{in} denotes the input representation derived from the learnable PE addition. The FFN module applies a two-layer linear transformation separated by a Gaussian Error Linear Unit (GELU) activation function and a dropout layer. The GELU activation function introduces a smooth non-linearity to capture complex electrochemical patterns effectively [60]. The dropout layer concurrently mitigates overfitting by randomly deactivating a designated fraction of neurons during the training phase [61,62]. Eq. (4) mathematically formulates this entire FFN computation.

$$H_{enc} = \text{LayerNorm}(\text{FFN}(H_{attn})) \oplus H_{attn} \tag{4}$$

where H_{enc} signifies the final output of a single transformer encoder layer, and FFN denotes the complete feed-forward network operation.

Following the internal transformer encoding sequence, the model utilizes a Scan-Level Attention Fusion mechanism (detailed comprehensively in the subsequent subsection) to squeeze the nine consecutive scans into a single, unified sequence representation. This condensed voltammetric feature vector is then directly fed into a specialized KAN regression head, which entirely replaces the conventional MLP module.

Unlike standard networks that apply fixed activation functions on the nodes, KANs—based on the Kolmogorov–Arnold representation theorem—fundamentally shift the learnable activation functions to the network edges. Consequently, to process these extracted signals, each output node j within the KAN layer acts merely as a summation point for the N_{in} incoming transformed features. This aggregation is mathematically formulated in Eq. (5) [63].

$$y_j = \sum_{i=1}^{N_{in}} \Phi_{j,i}(H_{fused}^{(i)}) + B_j \tag{5}$$

where $H_{fused}^{(i)}$ is the ith input feature extracted from the attention fusion, B_j is the regression bias term, and $\Phi_{j,i}(\cdot)$ denotes the learnable univariate function situated explicitly on the edge connecting input i to output j. While standard KANs typically parameterize $\Phi_{j,i}$ using B-splines, this study constructs these edge functions using parameterized Radial Basis Functions (RBF) to efficiently capture the extreme non-linearities of trace-level electrochemical signals. The continuous transformation for each specific edge function ($\Phi_{j,i}(H_{fused}^{(i)})$) is constructed by aggregating a predefined number of RBF centers (C), as mathematically formulated in Eq. (6) [63].

$$\Phi_{j,i}(H_{fused}^{(i)}) = \sum_{k=1}^{C} W_{j,i,k} \exp\left(-\left(\frac{H_{fused}^{(i)} - \mu_{i,k}}{\gamma_{i,k}}\right)^2\right) \tag{6}$$

Table 1
Structural search space and hyperparameter configurations of the iTransKAN architecture.

Component	Parameter	Search space
Inverted Tokenization	Projection dimension (d_{model})	{64, 128}
	Layer normalization	Applied
Transformer Encoder	Number of layers	{1, 2, 3}
	Attention heads	{4, 8}
	Feedforward dimension	$4 \times d_{model}$
	Activation function	GELU
	Dropout rate	{0.1, 0.2, 0.3}
Attention Fusion	Pooling mechanism	Multihead
KAN Regressor	Hidden layer dimension	{16, 32, 64}
	Output dimension	1
	RBF centers	[3, 7]

Table 2
Training optimization protocol and search space for the heavy metal quantification models.

Parameter	Search Space/Configuration
Tuning framework	Optuna (TPE Sampler, 100 trials)
Optimizer	AdamW
Base learning rate	{1e−4, 5e−4, 1e−3, 5e-3}
Weight decay	{1e−5, 1e−4, 1e-3}
Batch size	{8, 16, 32}
Learning rate scheduler	Cosine Annealing (T_{max} = 100)
Maximum epochs	100
Loss function	MSE
Gradient clipping	Max norm = 1.0
Weight initialization	Xavier Uniform (Linear layers)

Here, C represents the total number of RBF components per feature, while $\mu_{i,k}$ and $\gamma_{i,k}$ signify the dynamically updated center and width parameters for the kth basis of input i. Crucially, the parameter $W_{j,i,k}$ denotes the distinct learnable weight that maps the kth RBF activation from input i to the output node j. This specific tensor formulation allows each individual edge in the KAN module to independently learn highly complex, distinct non-linear mappings tailored to the voltammetric feature space prior to the final node aggregation.

Building upon this localized non-linear formulation, the KAN module functions as the final regression head within the broader framework. Instead of traditional B-splines, RBF are utilized as the core base functions in the KAN head. The utilization of RBF overcomes the recursive data dependencies inherent in B-splines, allowing each basis value to be computed independently [64]. Because RBF respond strongly only when the input is close to their centers, they provide a smooth and highly localized transformation [64]. This mathematical characteristic is exceptionally suited for voltammetric data, enabling the network to precisely map distinct electrochemical variations without the risk of surrounding background noise propagation. This theoretical advantage is empirically validated in Section 3.2, which demonstrates that the RBF-KAN configuration achieves significantly higher predictive accuracy than the spline-based implementation.

The complete architectural specifications, detailing the dimensions of the transformer encoder backbone and the sizing of the KAN layers, are summarized in Table 1. Given the complexity of this hybrid network, relying solely on fixed values from prior literature is insufficient. Therefore, a systematic hyperparameter tuning process was conducted using the Optuna framework to establish the optimal configuration. As outlined in Table 2, the optimization explored various search spaces over 100 trials utilizing the Tree-structured Parzen Estimator (TPE) algorithm. The final optimized model is trained using the AdamW optimizer with a Cosine Annealing scheduler across 100 epochs. This specific scheduling strategy is implemented to facilitate rapid initial exploration of the loss landscape, followed by a smooth, continuous decay that allows the localized parameters to stabilize into optimal minima without oscillating during the final training phases.

2.6. Proposed network refinements

The proposed iTransKAN framework implements two internal processing enhancements: (1) learnable PE and (2) scan-level attention fusion. These mechanisms are designed exclusively to accommodate the unique physical behaviors of multi-scan voltammetric sequences. The following subsections comprehensively detail these two architectural refinements.

2.6.1. Learnable positional encoding

Positional encoding (PE) mechanisms fundamentally inject crucial sequential order information into inherently permutation-invariant transformer architectures. Standard sinusoidal encodings mathematically generate fixed temporal representations based solely on absolute sequence indices. However, electrochemical multi-scan operations generate experimental measurements with complex chronological signal dependencies. Fixed sinusoidal functions lack the intrinsic mathematical flexibility to fully capture the non-linear data shifts occurring progressively across the sequential voltammetric cycles.

The proposed iTransKAN framework implements a learnable PE mechanism. This learnable PE adaptively optimizes a specialized multi-dimensional parameter tensor directly alongside the primary architectural weights. The encoding process operates through direct element-wise addition as modeled in Eq. (7).

$$H_{in} = H_{token} \oplus P_{learnable} \tag{7}$$

where H_{in} denotes the positionally encoded latent tensor matrix prepared for the transformer encoder, H_{token} represents the previously normalized scan tokens, and $P_{learnable}$ signifies the dynamically optimized positional weight array strictly matching the exact temporal sequence dimensions and latent spatial depth.

2.6.2. Scan-Level Attention Fusion

Scan-level data processing conceptually treats each CV scan as a distinct and unbroken informational unit. Attention fusion represents an advanced aggregation technique designed to dynamically weight and combine multiple scans based purely on their calculated contextual relevance. Standard sequence-based regression models typically generate final numerical predictions by blindly averaging all output tokens. This simple averaging mechanism severely dilutes critical analytical information present only within specific intermediate voltammetry scans.

The proposed iTransKAN framework overcomes this inherent limitation by implementing a specialized scan-level attention fusion module. This module operates according to Eq. (8).

$$H_{fused} = \text{Softmax}\left(\frac{Q_{learnable} \cdot K_{enc}^{T}}{\sqrt{d_{model}}}\right) \cdot V_{enc} \tag{8}$$

where H_{fused} represents the final aggregated and optimized sequence representation, $Q_{learnable}$ denotes the standalone learnable query vector acting as the attention guide, K_{enc} and V_{enc} signify the encoded key and value matrices mathematically derived from the preceding transformer encoder layers, and d_{model} indicates the constant numerical scaling factor corresponding to the latent dimension size.

The Scan-Level Attention Fusion effectively acts as a squeezing operation that compresses the entire multi-scan sequence into a single unified representation. This functional dimensionality reduction ensures exact structural compatibility with the subsequent KAN regression layers while preserving the most critical learned features.

2.7. Performance evaluation

Performance evaluation is a mandatory step within computational modeling pipelines. The primary objective of this evaluation is to quantify the predictive accuracy and statistical reliability of the proposed neural network framework. A comprehensive evaluation ensures highly objective comparisons against established benchmark deep learning algorithms. This study implements six common evaluation criteria specifically designed for continuous regression tasks. These metrics encompass the Coefficient of Determination (R^2), Mean Squared Error (MSE), Root Mean Squared Error (RMSE), Mean Absolute Error (MAE), Mean Absolute Percentage Error (MAPE), and Symmetric Mean Absolute Percentage Error (SMAPE) [37,38,65,66].

However, the six aforementioned metrics inherently assign identical mathematical penalties to both overestimated and underestimated concentration predictions. Toxicological threshold monitoring, in contrast, strictly requires an asymmetric evaluation framework that disproportionately penalizes underestimations. Underestimated heavy metal predictions pose exceptionally severe environmental and public health hazards compared to overestimations. For instance, predicting a heavy metal concentration below the actual toxicological threshold results in the erroneous classification of hazardous water as safe for consumption, which directly causes severe biological exposure. Conversely, an overestimation merely triggers unnecessary, albeit safe, preventative remediation. Consequently, this research introduces a novel evaluation metric designated as the Relative Asymmetric Toxicity Error (RATE). This metric deliberately imposes a significantly higher computational penalty upon hazardous underestimations while simultaneously maintaining relative evaluation fairness across widely varying levels of heavy metal concentrations. The RATE calculation operates mathematically according to Eqs. (9) and (10).

$$\mathrm{RATE} = \frac{1}{N}\sum_{i=1}^{N} \min\left(\frac{|Y_{true,i} - Y_{pred,i}|}{\max(|Y_{true,i}|, \tau)}, C\right) \cdot \Omega_i \tag{9}$$

$$\Omega_i = \begin{cases} \alpha, & \text{if } Y_{pred,i} < Y_{true,i} \\ 1, & \text{if } Y_{pred,i} \geq Y_{true,i} \end{cases} \tag{10}$$

where RATE represents the calculated Relative Asymmetric Toxicity Error, N denotes the total number of evaluated experimental samples, $Y_{true,i}$ indicates the actual heavy metal concentration derived from the laboratory preparation, and $Y_{pred,i}$ signifies the final concentration generated by the iTransKAN network. To prevent computational instability near the limit of detection, τ acts as a minimum denominator threshold (set to 1.0), while C serves as a capping constant (set to 10.0) to restrict extreme relative error outliers. Ω_i represents the conditional asymmetric penalty weight, and α denotes the predetermined strict amplification factor specifically applied to dangerous underestimations (where $\alpha > 1$).

Furthermore, to provide a holistic assessment of computational efficiency, this study evaluates three additional operational metrics. Training time measures the duration required to optimize model parameters, recorded in seconds (s). Inference time determines the speed of generating predictions during the testing phase, also measured in seconds (s). Lastly, memory usage captures the peak RAM allocation consumed throughout the computational process, expressed in megabytes (MB).

Beyond general predictive accuracy and computational efficiency, the practical viability of the proposed architecture for environmental deployment is further assessed through two specialized analytical protocols. First, to establish the fundamental sensory threshold, the Limit of Detection (LOD) and Limit of Quantification (LOQ) are calculated. Second, to evaluate the architecture's robustness against practical interferences in real-world water matrices, an independent external validation protocol is implemented. This assessment utilizes environmental water samples collected from ten distinct aquatic locations across Surabaya, Indonesia. These samples are systematically spiked with varying trace-level concentrations of Pb and Cd. By evaluating the model on this independent dataset, the analysis effectively verifies the network's generalization capability, ensures the absence of overfitting to the primary laboratory data, and confirms its capacity to maintain predictive stability when subjected to actual physical and chemical interferences in complex aquatic environments.

3. Results and discussion

This section provides an evaluation of the proposed chemometric framework for heavy metal quantification. The discussion begins with a performance analysis of the iTransKAN architecture. Subsequently, an ablation study is presented to validate the individual contributions of the integrated network refinements. Following this, the Limit of Detection (LOD), Limit of Quantification (LOQ), and the model's robustness in real-world water matrices are evaluated. Finally, the practical safety and efficacy of the framework are assessed using the novel RATE metric.

3.1. Performance analysis of iTransKAN

The systematic validation of the proposed architecture is structured into three comprehensive analytical phases to rigorously assess its robustness and accuracy. First, Section 3.1.1 presents an extensive benchmarking of iTransKAN against six established deep learning models. Subsequently, Section 3.1.2 quantifies the absolute performance gain achieved by transitioning from classical chemometric algorithms to the deep learning approach. Finally, Section 3.1.3 presents the statistical validation and uncertainty quantification for the proposed iTransKAN model.

3.1.1. Comparison with deep learning architectures

Performance benchmarking evaluates the proposed iTransKAN architecture against six established deep learning models. Fig. 4 details the comparative evaluation results across both Pb and Cd analytes.

The evaluation begins by comparing the input data formats. Fig. 4 shows that continuous raw voltammetric data generate lower error rates than frequency-domain data across the tested network architectures and metal types. Raw data preserve the complete current profiles and subtle background variations. Conversely, while FFT isolates principal frequency components, this spectral transformation discards time-domain electrochemical context. For Pb detection, the iTransKAN model utilizing raw data achieves an RMSE of 5.16. The identical architecture processing frequency-domain data yields an RMSE of 12.01. This difference represents a 57.00% error reduction when using raw inputs. Similar improvements appear in other metrics, where the raw data reduce MAE by 55.31% (from 6.6 to 2.9). For Cd detection, the raw data approach similarly produces lower error values compared to the frequency-domain inputs. Specifically, the raw data configuration achieves an RMSE of 39.14 and an MAE of 15.0, corresponding to error reductions of 12.86% and 8.76% relative to the FFT data. These consistent reductions across both analytes suggest that preserving the temporal context of complete multi-scan data provides a more suitable input for the proposed framework than spectral extraction.

Within the raw data configuration, the iTransKAN framework shows lower prediction errors compared to the baseline deep learning architectures. For Pb detection, the network records an R^2 of 0.9997, compared to the baseline iTransformer value of 0.9977. The addition of the KAN regression head corresponds with lower absolute prediction deviations, achieving an MAE of 2.9. This represents a 72.22% error reduction compared to the standard iTransformer MAE of 10.6. The proposed architecture also yields an SMAPE of 19.50%, a 47.43% relative decrease over the iTransformer (37.08%). Furthermore, standard recurrent neural networks such as LSTM and BiGRU produce SMAPE values exceeding 50% on the same dataset.

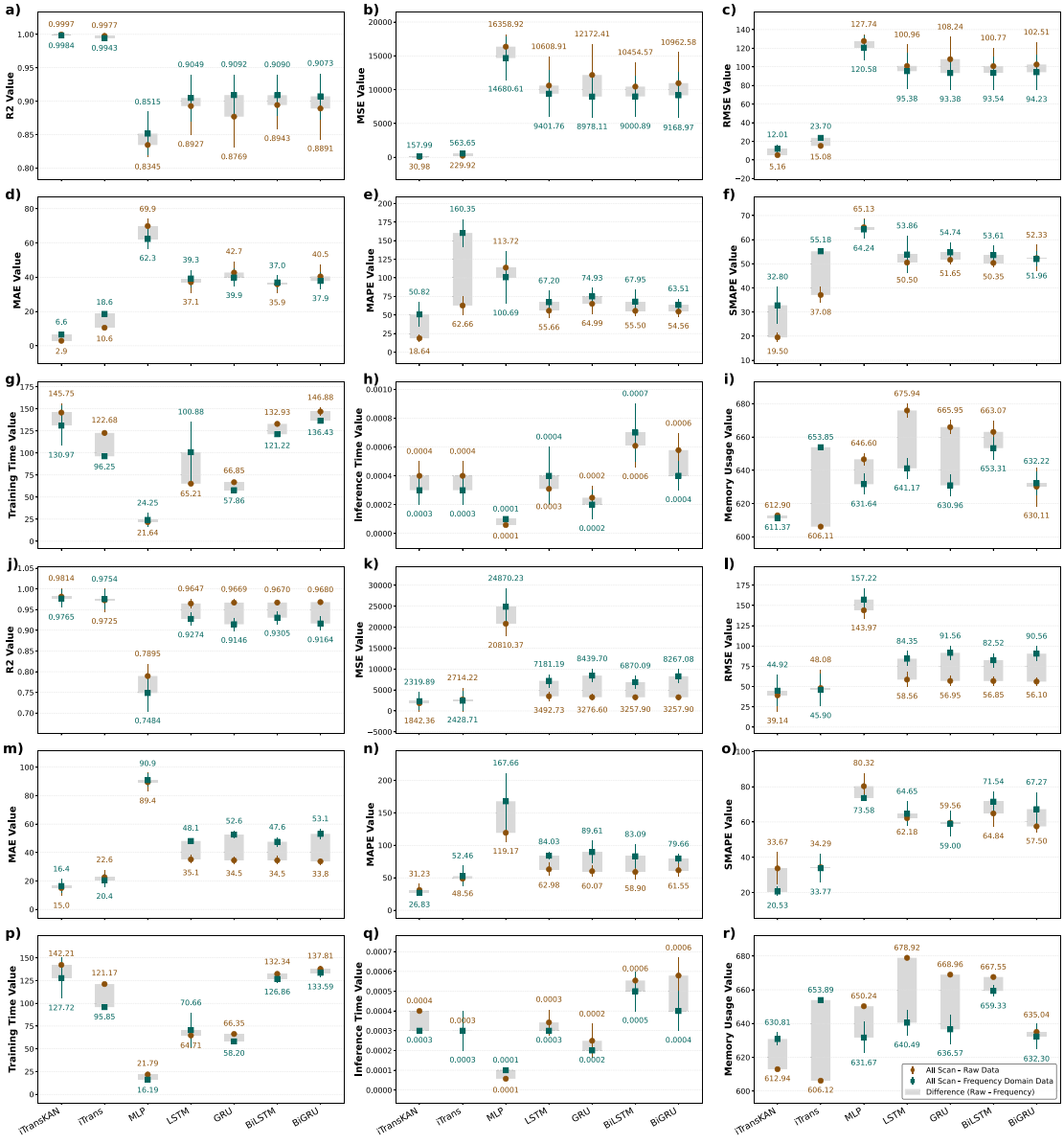

Fig. 4. Comprehensive performance comparison of the proposed iTransKAN and baseline architectures across varying input configurations for Pb (a–i) and Cd (j–r) quantification. The transparent gray spans explicitly illustrate the performance gap between the raw and frequency-domain input representations, while the vertical error bars indicate the standard deviation across cross-validation.

For Cd detection, which involves more complex signal interference, the iTransKAN model maintains a similar trend. When processing raw Cd measurements, it achieves an R^2 of 0.9814, compared to the baseline iTransformer's 0.9725. The framework records an MAE of 15.0 and an SMAPE of 33.67%, representing error reductions of 33.78% and 1.81%, respectively, over the standard iTransformer. Conventional MLPs show limitations with this temporal data structure, recording an R^2 of 0.7895 and an SMAPE of 80.32%. Recurrent architectures like BiGRU perform better than MLPs but still exhibit an SMAPE of 57.50%. Compared to the BiGRU, iTransKAN reduces the SMAPE by 41.45%.

Regarding computational requirements, the iTransKAN model utilizing raw data requires the highest training time (145.75 s for Pb and 142.21 s for Cd) among the evaluated deep learning models. This longer duration is a trade-off for the global sequence modeling performed by the iTransformer backbone. However, the model maintains an efficient memory usage (612.90 MB for Pb and 612.94 MB for Cd). This memory consumption remains noticeably lower than standard dense MLPs (646.60 MB for Pb) and heavily gated recurrent networks. This memory efficiency relates to the inverted tokenization strategy, which embeds entire time series as single tokens. Regarding practical deployment, iTransKAN records an inference time of 4.0×10^{-4} s per sample for both Pb and Cd. Because this duration is on a sub-millisecond scale, processing incoming multi-scan data in real-time embedded systems remains feasible.

3.1.2. Comparison with classical chemometrics

A rigorous quantification of the actual performance gain achieved by adopting the deep learning paradigm is presented by explicitly benchmarking the proposed iTransKAN against classical chemometric methods traditionally utilized in electroanalysis: Partial Least Squares (PLS) and Principal Component Regression (PCR). Table 3 summarizes the comprehensive predictive and computational metrics for these algorithms.

The quantitative evaluation reveals a significant predictive disparity. Using raw multi-scan data, classical algorithms exhibit poor

Table 3
Comprehensive performance comparison between iTransKAN and classical chemometric models using raw and frequency-domain data.

Target	Dataset	Model	R^2	MSE	RMSE	MAE	MAPE (%)	SMAPE (%)
Pb	Raw Data	**iTransKAN**	**0.9997**	**30.98**	**5.16**	**2.9**	**18.64**	**19.50**
		PLS	−0.3153	130 039.15	291.44	138.1	367.96	89.25
		PCR	0.5956	39 982.13	198.61	133.4	488.35	92.47
	Frequency-domain Data	iTransKAN	0.9984	157.99	12.01	6.6	50.82	32.80
		PLS	0.5718	42 328.98	202.58	117.9	544.10	85.64
		PCR	0.4933	50 096.77	222.99	140.7	618.23	92.12
Cd	Raw Data	**iTransKAN**	**0.9814**	**1842.36**	**39.14**	**15.0**	**31.23**	**33.67**
		PLS	0.5339	46 078.93	212.08	144.1	888.65	96.78
		PCR	0.4020	59 116.04	243.03	177.1	1320.19	99.55
	Frequency-domain Data	iTransKAN	0.9765	2319.89	44.92	16.4	26.83	20.53
		PLS	0.3102	68 195.52	258.09	167.5	997.59	98.54
		PCR	0.2254	76 581.41	276.73	221.9	1714.18	117.41

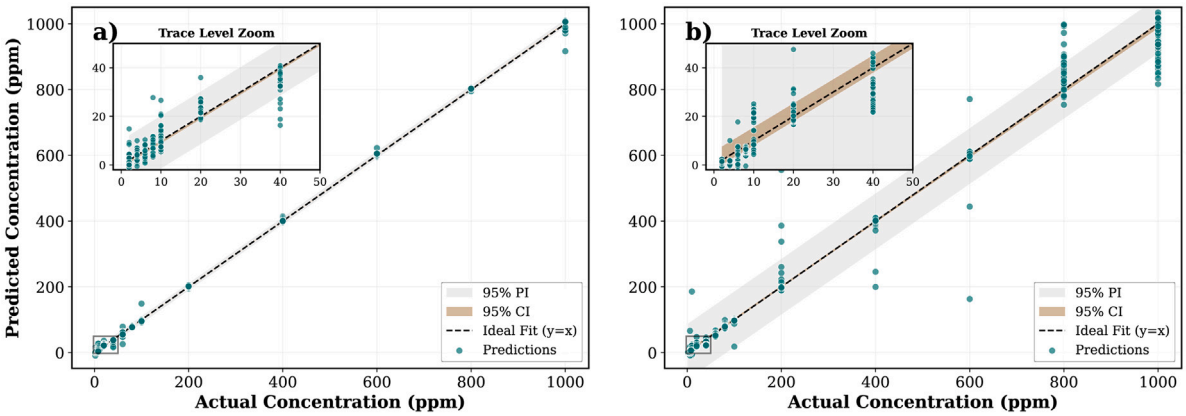

Fig. 5. Actual versus predicted concentration plots featuring 95% confidence intervals (CI) and prediction intervals (PI) for (a) Pb and (b) Cd.

accuracy. For Pb quantification, PLS and PCR record MAE values of 138.1 and 133.4, respectively, while iTransKAN achieves a minimal MAE of 2.9. Similarly, in the Cd detection task, the best-performing classical model (PLS) yields an MAE of 144.1, whereas iTransKAN reduces this to 15.0. To explicitly quantify the gain from the deep learning approach, iTransKAN reduces the MAE by 97.8% for Pb (compared to PCR) and by 89.6% for Cd (compared to PLS). This performance gain is further corroborated by the RMSE metrics, where the proposed iTransKAN architecture decreases the error margin by over 81% across both analytes. Because PLS and PCR rely strictly on linear multivariate projections, they are completely overwhelmed by the highly nonlinear and complex nature of the electrochemical data.

3.1.3. Statistical validation and uncertainty quantification

Statistical validation and uncertainty quantification were performed to evaluate the reliability of the proposed iTransKAN framework. For this final evaluation, the continuous raw multi-scan data was utilized as the primary input, given its demonstrated superiority over frequency-domain data across the majority of tested architectures. A Wilcoxon signed-rank test comparing the absolute errors of iTransKAN against the baseline models yielded a p-value of 2.25×10^{-93} for Pb and 7.13×10^{-49} for Cd ($p < 0.001$). This result indicates that the performance improvements achieved by the proposed architecture are statistically significant, particularly when compared to the standard iTransformer, which serves as the second-best performing method in this study.

To further visualize this statistical reliability and assess predictive uncertainty, Fig. 5 presents the actual versus predicted concentration plots, incorporating 95% Confidence Intervals (CI) and Prediction Intervals (PI). The inner shaded region (CI) represents the certainty of the regression fit. For Pb quantification, the average 95% CI width is 1.21 ppm. Due to this narrow width, the CI in the primary Pb plot is visually covered by the regression line, indicating low uncertainty in the model's global predictive trend. For Cd, the average 95% CI width is 9.45 ppm, which is visible in the zoomed-in inset. These narrow confidence bounds suggest that the model's regression parameters are stable across the tested concentrations.

The 95% Prediction Interval (PI) bounds the expected variance for individual target predictions. For Pb, the average 95% PI width is 21.60 ppm, meaning individual predictions typically vary by approximately ± 10.80 ppm from the estimated value. For Cd, the average 95% PI width is 168.83 ppm (± 84.41 ppm). The wider interval for Cd is expected due to the highly complex and overlapping nature of its concentration data. However, these uncertainty margins remain acceptable given the dataset's wide operational measurement range, which spans from trace levels up to 1000 ppm.

3.2. Ablation study

An ablation study systematically deconstructs the iTransKAN architecture to quantify the distinct mathematical contribution of individual network modules. Table 4 details this comprehensive analysis across six configurations (Models A1–A6), systematically isolating the Learnable PE, Scan-Level Attention Fusion, and KAN regressor. Given that continuous raw data consistently outperformed frequency-domain data in the previous evaluation, the raw dataset was selected as the exclusive input format for this ablation framework.

Fig. 6 presents a residual analysis to further compare the predictive performance of the evaluated configurations. The scatter plots show that the complete architecture (Model A1) minimizes extreme outliers for both Pb and Cd targets. For instance, Model A1 constrains the Pb prediction errors within a boundary of approximately ±75 ppm. In

Table 4
Comprehensive ablation study results evaluating individual architectural components on the raw continuous dataset.

Target	Model	Configuration	Learnable PE	Scan-Level Fusion	KAN	R^2	MSE	RMSE	MAE	MAPE (%)	SMAPE (%)
Pb	**iTransKAN**	A1	✓	✓	✓	**0.9997**	**30.98**	**5.16**	**2.9**	**18.64**	**19.50**
	iTransKAN	A2	✓	×	✓	0.9994	56.42	7.27	4.6	27.96	28.97
	iTransKAN	A3	×	✓	✓	0.9994	54.58	6.45	3.1	31.63	18.01
	iTransformer	A4	✓	✓	×	0.9993	70.03	8.30	5.3	33.71	30.31
	iTransformer	A5	✓	×	×	0.9990	101.95	9.94	6.2	40.90	30.97
	iTransformer	A6	×	✓	×	0.9947	520.02	17.33	6.7	21.89	19.76
Cd	**iTransKAN**	A1	✓	✓	✓	**0.9814**	**1842.36**	**39.14**	**15.0**	**31.23**	**33.67**
	iTransKAN	A2	✓	×	✓	0.9809	1889.84	39.34	16.0	41.99	35.92
	iTransKAN	A3	×	✓	✓	0.9729	2677.58	46.58	21.9	64.91	32.88
	iTransformer	A4	✓	✓	×	0.9788	2098.56	42.11	15.5	29.58	24.42
	iTransformer	A5	✓	×	×	0.9730	2673.62	45.34	16.9	31.01	26.12
	iTransformer	A6	×	✓	×	0.9777	2208.67	44.31	20.6	42.26	27.04

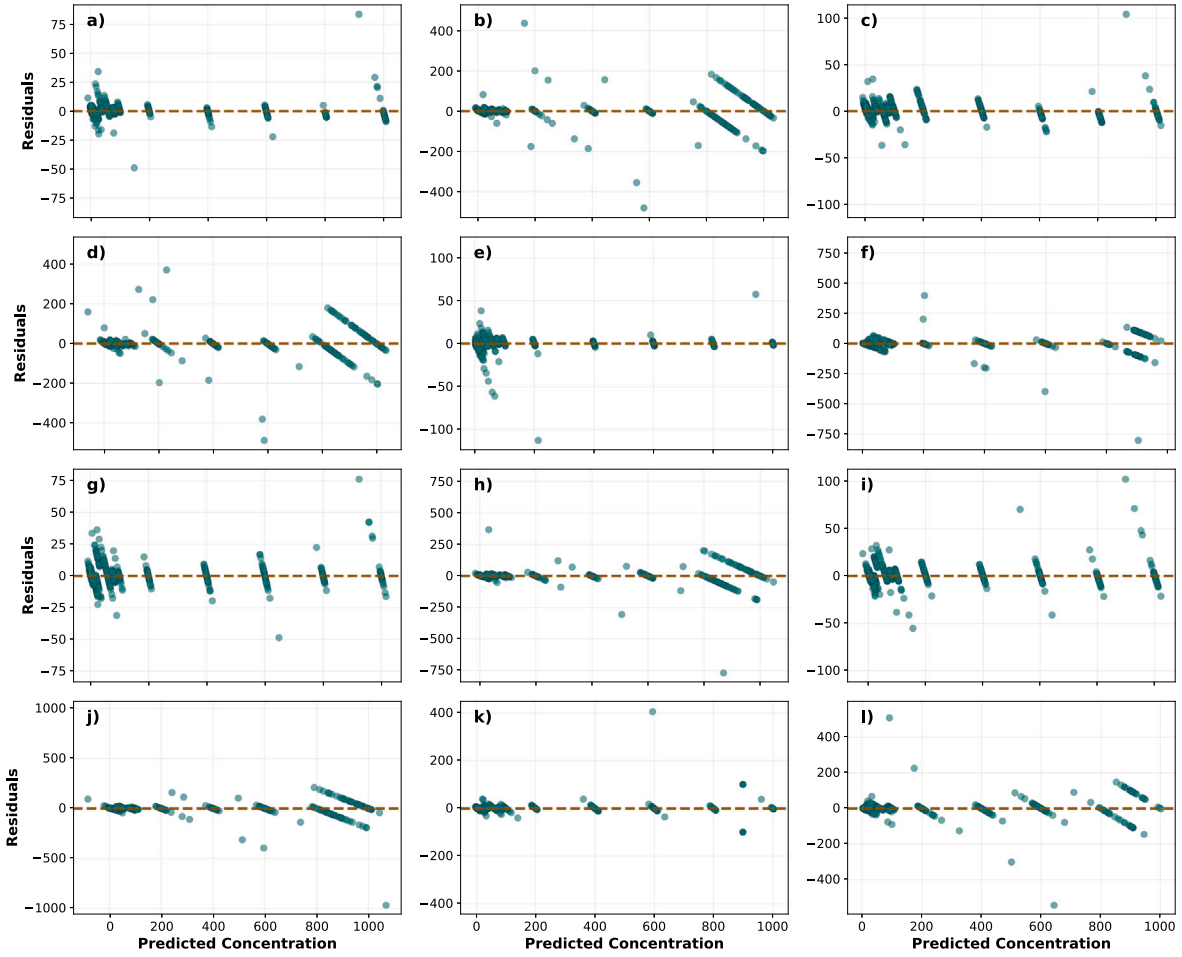

Fig. 6. Residual analysis for the evaluated ablation architectures (Models A1–A6). The scatter plots display the prediction residuals against predicted concentrations for Pb (a–f) and Cd (g–l).

contrast, removing the KAN and Transformer components (e.g., Model A4) increases this error margin, resulting in scattered outliers that exceed ±400 ppm. This visual evidence indicates that the complete iTransKAN architecture (A1) provides the most stable predictions. The specific contribution of each component is analyzed in the following subsections.

3.2.1. Impact of the KAN regression head

The integration of the KAN regression head yields substantial predictive improvements across the sequence-modeling architecture. For Pb quantification, the standard iTransformer equipped with all attention refinements (Model A4) produces an MAE of 5.3. Substituting the

Table 5
Performance comparison of the KAN regression head utilizing RBF versus B-Spline base functions.

Target	Basis function	R^2	MSE	RMSE	MAE	MAPE (%)	SMAPE (%)
Pb	RBF	**0.9997**	**30.98**	**5.16**	**2.9**	**18.64**	**19.50**
	Spline	0.9996	41.04	6.41	4.1	46.12	20.87
Cd	RBF	**0.9814**	**1842.36**	**39.14**	**15.0**	**31.23**	**33.67**
	Spline	0.9807	1906.37	43.66	32.3	158.03	61.28

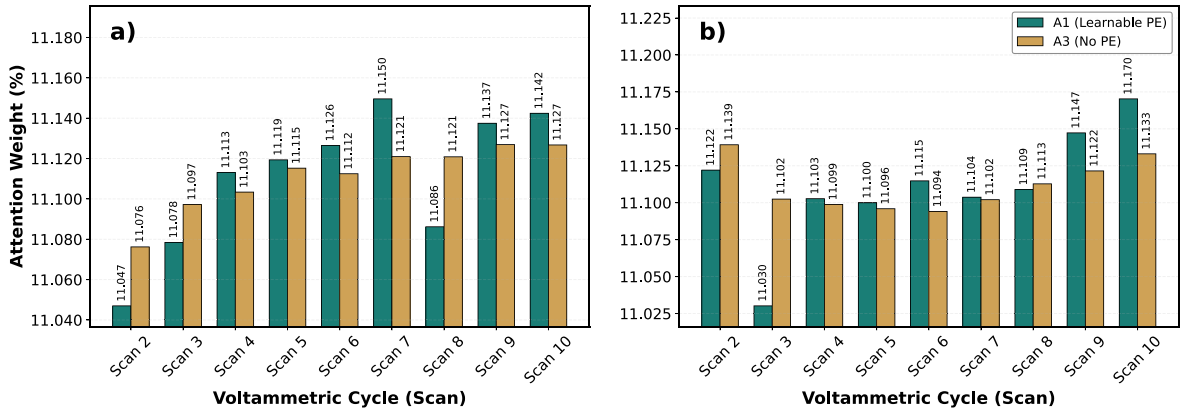

Fig. 7. Attention weight distributions across voltammetric scans for (a) Pb and (b) Cd. The learnable PE (Model A1) adaptively differentiates weighting patterns across sequential cycles, whereas omitting the positional embedding (Model A3) results in a more restricted and uniform distribution.

Table 6
Performance degradation analysis based on the number of inputted voltammetric measurement cycles (scans).

Target	Cycles	R^2	MSE	RMSE	MAE	MAPE (%)	SMAPE (%)
	10	**0.9997**	**30.98**	**5.16**	**2.9**	**18.64**	**19.50**
Pb	5	−0.0002	98 886.66	314.46	252.7	1770.05	128.98
	3	−0.0010	98 964.23	314.59	250.3	1726.15	128.69
	10	**0.9814**	**1842.36**	**39.14**	**15.0**	**31.23**	**33.67**
Cd	5	−0.0003	98 895.98	314.48	252.3	1762.58	128.93
	3	−0.0007	98 932.57	314.54	251.1	1740.62	128.79

standard regression head with the specialized KAN module (Model A1) significantly reduces this metric to 2.9, representing a clear reduction in absolute prediction error. The Cd analysis mirrors this performance trend, where the KAN integration effectively decreases the Cd MAE from 15.5 (A4) down to 15.0 (A1). This consistent error minimization demonstrates the superior non-linear mapping capabilities of KAN during complex concentration calibrations. Furthermore, the magnitude of improvement observed in the MAE is proportionally reflected across all other evaluated metrics (including R^2, MSE, RMSE, and SMAPE), confirming a consistent and comprehensive enhancement in the model's global accuracy.

To further optimize this regression head, an internal configuration analysis was conducted comparing the RBF and B-Spline as the core base functions for the KAN module, as detailed in Table 5. The evaluation demonstrates that the RBF configuration is superior for voltammetric data processing. Using the RBF, the model restricts the MAE to 2.9 for Pb and 15.0 for Cd. In contrast, utilizing the B-Spline function increases the error margins, yielding a higher MAE of 4.1 for Pb and expanding significantly to 32.3 for Cd. The RBF's ability to localize and map specific nonlinearities inherently matches the localized peak characteristics of electrochemical signals much better than the continuous polynomial segments of B-Splines

3.2.2. Effectiveness of scan-level attention fusion

The proposed scan-level attention fusion mechanism constitutes an important performance component within the iTransKAN framework. Transitioning from standard sequence averaging (Model A2) to the scan-level fusion module (Model A1) yields a notable enhancement in analytical precision. For Pb quantification, this architectural modification minimizes the MAE from 4.6 down to 2.9. The Cd analysis corroborates this positive trend, demonstrating a parallel MAE reduction from 16.0 (A2) to 15.0 (A1). This performance gain indicates that the attention-based mechanism effectively extracts crucial temporal variations embedded within specific intermediate voltammetric cycles, whereas simple arithmetic averaging is less effective at isolating these electrochemical signals.

The effectiveness of this attention fusion is dependent on the amount of sequential data provided, as demonstrated in Table 6. An evaluation comparing the input lengths of 10, 5, and 3 cycles reveals that utilizing the complete 10-scan sequence is a necessary configuration for maintaining model stability. For the Pb target, reducing the input sequence from 10 scans to 5 and 3 scans leads to a severe inflation of error margins, causing the MAE to expand from 2.9 to 252.7 and 250.3, respectively, alongside negative R^2 values. Similarly, for the Cd target, limiting the measurement history increases the MAE from 15.0 (10 scans) to 252.3 (5 scans) and 251.1 (3 scans). These outcomes indicate that truncating the measurement cycles discards vital temporal information, which the sequence-modeling architecture requires to execute reliable electrochemical calibration.

3.2.3. Role of the learnable positional embedding

Beyond the KAN regression head and the attention-based fusion, the learnable PE matrix serves as another important component of the architecture. Upgrading from a model variant omitting positional information (Model A3) to the dynamic learnable positional embedding of the complete iTransKAN framework (Model A1) enhances predictive stability. For the Pb target, the inclusion of this learnable PE reduces the MAE from 3.1 to 2.9. The Cd analysis exhibits a more pronounced accuracy gain, where the MAE decreases from 21.9 down to 15.0. This performance difference suggests that tracking the relative position of individual cycles within the voltammetric sequence is highly beneficial. Without positional tracking, Model A3 treats all scans identically and ignores their order in the sequence. In contrast, the learnable PE in Model A1 introduces sequence awareness, enabling the framework to assign different attention weights to each scan based on its specific position.

This sequence-mapping capability is further illustrated by the attention distribution weights presented in Fig. 7. When processing both targets, Model A3 (without PE) displays a highly restricted and static allocation of attention weights across the voltammetric cycles. This flat or marginally shifting pattern indicates that without positional tracking, the network lacks the structural awareness to selectively

Table 7
External validation performance of the iTransKAN model on independent environmental water samples.

Target	Evaluation Dataset	R^2	MSE	RMSE	MAE	MAPE (%)	SMAPE (%)
Pb	Real-World Water (Spiked 2–10 ppm)	0.9726	0.22	0.47	0.4	10.58	10.52
Cd	Real-World Water (Spiked 2–10 ppm)	0.8040	1.57	1.25	0.9	17.12	21.62

prioritize specific segments of the scan sequence. In contrast, Model A1, equipped with the learnable PE, demonstrates a highly dynamic and responsive weight distribution. Its attention profile exhibits significant and sharp fluctuations, characterized by prominent decreases followed by steep, rapid climbs across successive scans. This distinct behavioral divergence demonstrates that the complete framework effectively leverages explicit sequence position to adaptively focus its attention, thereby enhancing the quantification performance.

3.3. Limit of detection and quantification

Based on the standard IUPAC calculations, the iTransKAN model demonstrates high sensitivity for the Pb target, achieving a LOD of 0.81 ppm and a LOQ of 2.45 ppm. For the Cd analyte, the LOD and LOQ are determined to be 6.38 ppm and 19.32 ppm, respectively. The higher threshold values for Cd compared to Pb are directly attributed to the complex and irregular signal patterns across different concentration levels within the raw voltammetric data.

Furthermore, an evaluation at the low boundary concentration of 2 ppm indicates the practical reliability of the model for environmental monitoring. At 2 ppm, iTransKAN records constrained error margins, yielding a MAE of 2.05 and a RMSE of 3.20 for Pb. Similarly, for Cd, the model maintains a MAE of 1.45 and an RMSE of 1.82. These evaluation metrics indicate that iTransKAN preserves stable and accurate predictive capabilities even when operating near the detection limits.

3.4. Real-world environmental validation

The independent external validation, utilizing environmental water samples from distinct locations in Surabaya, directly assesses the proposed architecture's generalization capability under practical sensing conditions. Table 7 presents the predictive performance of the optimized iTransKAN model on this real-world dataset, which is spiked with trace-level concentrations (2.0 to 10.0 ppm) of Pb and Cd.

As shown in Table 7, the iTransKAN architecture successfully predicts the trace-level concentrations despite the presence of complex environmental interferences. For Pb quantification, the model achieves an R^2 of 0.9726, indicating a strong correlation with the true spiked concentrations. The absolute deviations remain constrained, yielding an MAE of 0.4 ppm and an RMSE of 0.47 ppm.

For Cd detection, which inherently experiences higher susceptibility to overlapping background signals in real matrices, the model demonstrates acceptable predictive stability. It records an R^2 of 0.8040, accompanied by an MAE of 0.9 ppm and an RMSE of 1.25 ppm. The ability of iTransKAN to maintain these error margins on external samples indicates that the network does not exhibit severe overfitting to the primary laboratory dataset. These outcomes verify that the architecture effectively isolates the target analyte signals from actual physical and chemical interferences in complex aquatic environments.

3.5. RATE evaluation and visualization

Evaluation of the proposed framework relies on the RATE metric to verify safety and reliability. Unlike standard symmetric error measurements, RATE applies an asymmetric penalty on under-predictions, which are inherently more dangerous in environmental monitoring where undetected heavy metals pose severe health risks. To address the selection of the penalty factor (α), this study implements a sensitivity analysis using $\alpha = 2$ (mild caution), $\alpha = 5$ (moderate penalty), and $\alpha = 10$ (strict regulatory compliance). Fig. 8 details the performance of configurations A1–A6 across these varying factors. The axes represent specific concentration targets, and the plotted dimensions reflect the RATE scores on a logarithmic radial scale. A smaller enclosed area denotes superior and more stable predictive performance across the concentration spectrum. Model A1 appears almost invisible at the center origin across all subplots, indicating that the full proposed refinement effectively minimizes prediction errors regardless of penalty severity.

The ablation variants (A2–A6) all exhibit substantial error expansion relative to A1, with RATE scores climbing sharply at low concentration targets. Among these, A3 records the most severe degradation, followed closely by A4, A5, and A6, each registering near-maximum scores along multiple radial axes — particularly at low Pb concentration targets where accurate detection is most critical. These large enclosed polygons collectively demonstrate that the removal of any key network component leads to systematic under-prediction of heavy metal concentrations, undermining the model's reliability as a safety-critical monitoring tool.

The comparison across α values explicitly demonstrates the model's sensitivity to this penalty choice. At $\alpha = 2$ (Fig. 8a, 8d), the concentration target range spans 0–10 ppm for both Pb and Cd, and the polygon areas for A2–A6 already show clear deviations from the origin. As the penalty escalates to $\alpha = 10$ (Fig. 8c, 8f), the radial coverage of concentration targets expands to 0–24 ppm for Pb and 0–14 ppm for Cd, and the error footprints of ablation variants expand dramatically outward — pushing toward the scale ceiling of 1000. The extreme penalty factor forces even minor under-estimations into massive error spikes. In sharp contrast, the iTransKAN with full proposed refinement exhibits zero expansion despite this α increase, maintaining its position at the origin across all conditions. Crucially, while RATE heavily penalizes under-estimation during evaluation, it does not induce a systematic overprediction bias within the network. This risk is fundamentally controlled by utilizing the MSE as the loss function during training (as established in Table 2). RATE thus functions purely as a post-hoc evaluation metric to confirm environmental safety, ensuring the architecture remains highly accurate without artificially inflating its predictions.

3.6. Comparison with previous research

The proposed iTransKAN model achieves optimal performance during the detection of lead (Pb) concentrations. To benchmark its effectiveness, this section presents a comparison with recent studies that also detect Pb across different environmental samples such as water, soil, dust, and leaves. Table 8 outlines the algorithms and error metrics from these prior investigations. Previous research utilizes various ML/DL approaches, from standard Linear Regression to complex CAFF and Histogram-based Gradient Boosting algorithms.

The comparative analysis highlights the strong performance of the iTransKAN model. The proposed architecture records an RMSE of 5.16, an MAE of 2.93, and a MAPE of 18.64. These values represent the lowest error margins across almost all evaluation metrics compared to the discussed studies. For instance, while the Group Method of Data Handling (GMDH) algorithm applied to dust samples achieves a slightly lower RMSE of 2.87, the iTransKAN model demonstrates superior overall consistency by maintaining exceptionally low MAE and MAPE scores, which are critical for trace-level evaluation. Furthermore,

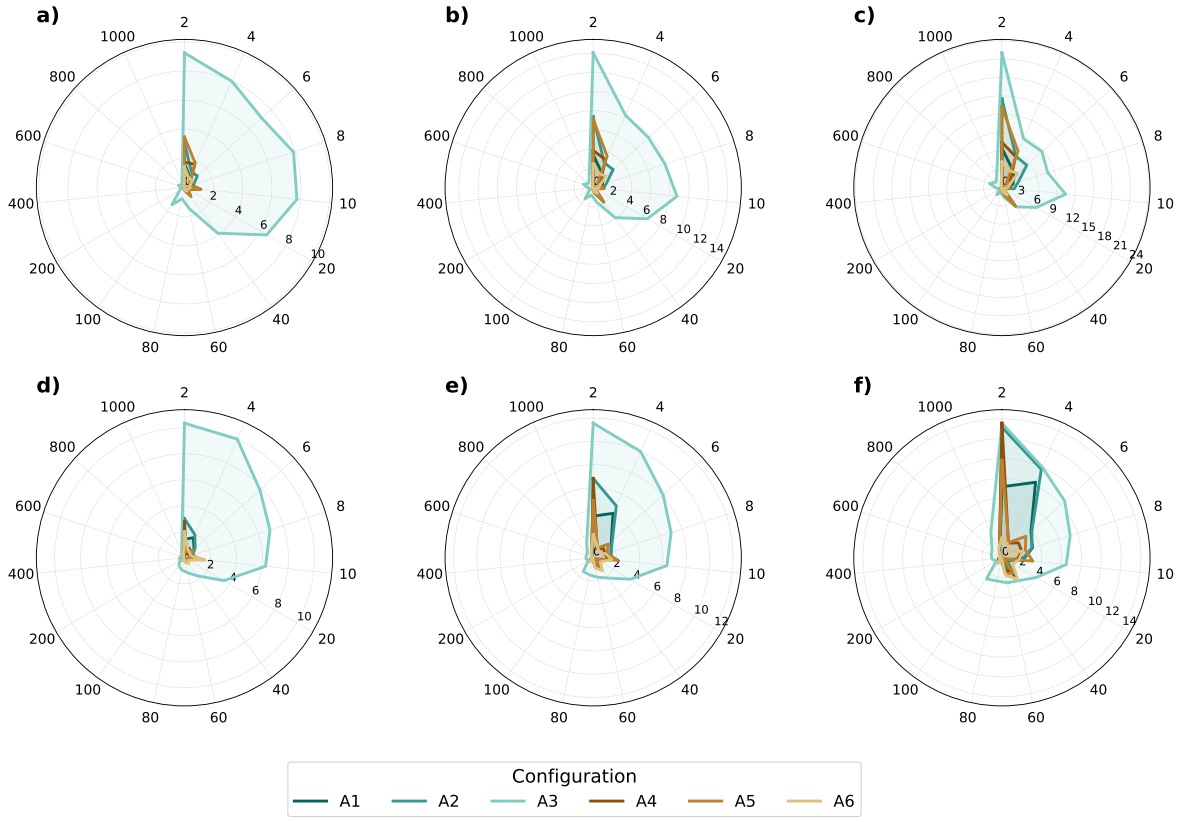

Fig. 8. Radar plots comparing the RATE of configurations A1–A6 across varying concentration targets. Performance is evaluated for Pb (a–c) and Cd (d–f) under penalty factors $\alpha = 2$ (a, d), $\alpha = 5$ (b, e), and $\alpha = 10$ (c, f). The axes represent specific concentration targets, and the plotted dimensions reflect the RATE scores.

Table 8
Comparison of ML/DL algorithms for Pb detection across various environmental samples.

Author	Sample	Algorithm	RMSE	MAE	MAPE
[39]	Water	Cross-Attention Feature Fusion (CAFF)	–	7.45	54.53
[67]	Soil	Histogram-based Gradient Boosting	7.95	–	–
[68]	Dust	Group Method of Data Handling (GMDH)	2.87	–	–
[69]	Leaves and road dust	SVM - Multiple	125.10	71.81	–
[70]	Water	Linear Regression	215.42	182.19	–
Proposed Study	Water	**iTransKAN**	5.16	2.93	18.64

the iTransKAN approach significantly reduces the mean absolute percentage error to 18.64. This represents a profound improvement over the 54.53 MAPE recorded by the earlier Cross-Attention Feature Fusion (CAFF) method evaluated on similar water samples. These precise results validate the capability of the iTransKAN algorithm for accurate Pb quantification.

4. Conclusion

This study establishes the novel iTransKAN framework for precise heavy metal quantification. The proposed methodology explicitly processes continuous multi-scan voltammetric data to capture temporal signal variations across sequential cycles. Comprehensive evaluations demonstrate the performance advantage of the proposed framework over six established baseline neural networks. The iTransKAN architecture consistently outperforms the standard iTransformer baseline, yielding a 72.2% reduction in Mean Absolute Error (MAE) for Pb and a 33.8% reduction for Cd. The full proposed refinement equipped with learnable PE and scan-level attention fusion achieves a robust R^2 of 0.9997 (95% CI: 0.9993–1.0000) for Pb and 0.9814 (95% CI: 0.9570–1.0000) for Cd. The systematic ablation study verifies that every structural component directly restricts prediction variance and prevents temporal signal degradation. This structural integrity is further confirmed by the RATE metric evaluation, where the iTransKAN with the proposed refinement successfully prevents hazardous concentration under-predictions.

This study demonstrates the model's predictive accuracy and quantitative resilience against simulated noise representing real-world matrix interferences. Furthermore, because the iTransKAN framework acts as a universal model that learns representations directly from data without relying on hard-coded electrochemical equations, it exhibits high generalizability. Future research will explore extending this architecture to a broader range of analytes, such as organic contaminants, and adapting it to process data from other detection techniques like Atomic Absorption Spectroscopy (AAS) or Inductively Coupled Plasma (ICP) to broaden its utility in analytical chemistry.

CRediT authorship contribution statement

Fadlilatul Taufany: Writing – original draft, Validation, Methodology, Formal analysis, Conceptualization. **Rizqy Ahsana Putri:** Writing – review & editing, Validation, Methodology, Data curation. **Riyanarto Sarno:** Writing – review & editing, Supervision, Investigation. **Wahyu Prasetyo Utomo:** Visualization, Software, Formal analysis. **Kelly Rossa Sungkono:** Resources, Project administration, Funding acquisition. **Arif Abdullah Sagran:** Visualization, Validation.

Declaration of competing interest

The authors declare that they have no known competing financial interests or personal relationships that could have appeared to influence the work reported in this paper.

Acknowledgments

This research is funded by the Indonesian Endowment Fund for Education (LPDP) on behalf of the Indonesian Ministry of Higher Education, Science and Technology and managed under the EQUITY Program (Contract No 4299/B3/DT.03.08/2025 & No 3029/PKS/ITS/2025).

Data availability

The complete source code implementation supporting the findings of this study is publicly available in the GitHub repository at https://github.com/ahsnputri/iTransKAN.

References

[1] Y. Zhou, M. Chen, AI-driven chemometric deep learning for monitoring oxidative degradation in polymer sports protective materials, Microchem. J. (2026) http://dx.doi.org/10.1016/j.microc.2026.117605.

[2] A. Cunha Paiva, G.A. Passos de Resende, L.D. Barbosa, D.L. Dantas Freitas, G.P. Sabin, L.W. Hantao, Quality assessment of Brazilian olive oils by GC× GC–MS and chemometrics, Anal. Bioanal. Chem. (2026) http://dx.doi.org/10.1007/s00216-026-06321-8.

[3] S. Chen, AI-based analytical chemistry and smart chemometric computing for multisensor detection of chemical compounds in environmental systems, Microchem. J. (2026) http://dx.doi.org/10.1016/j.microc.2026.117637.

[4] B.S. Bansod, M. Antil, Stripping voltammetry meets chemometric: a powerful duo for pinpointing harmful As3+ ions in water, J. Appl. Electrochem. 55 (2) (2025) 409–419, http://dx.doi.org/10.1007/s10800-024-02178-w.

[5] B.S. Bansod, M. Antil, Chemometric analysis of voltammetric-based sensing of heavy metal ions in aqueous solution for lead (Pb+2) ions, J. Indian Chem. Soc. 100 (10) (2023) 101083, http://dx.doi.org/10.1016/j.jics.2023.101083.

[6] D.S. Ferreira, R.A. Silva, G.M. Pacheco, E.R. Pereira-Filho, F.M.V. Pereira, A review of multivariate modelling for x-ray fluorescence techniques, Chemometr. Intell. Lab. Syst. 271 (2026) 105663, http://dx.doi.org/10.1016/j.chemolab.2026.105663.

[7] N. Mia, M.A. Hashem, M.A. Halim, S. Tariq, Z. Ahamed, Application of NIR spectroscopy with machine learning in the food industry: A comprehensive review, Food Phys. 3 (2026) 100089, http://dx.doi.org/10.1016/j.foodp.2026.100089.

[8] H. Guo, K. Grover, E.J. New, Machine learning assisted fluorescent sensor array for sensing applications, Adv. Sens. Res. 5 (2) (2026) e00172, http://dx.doi.org/10.1002/adsr.202500172.

[9] G. Hamideh, E. Mojgan, Assessment of groundwater vulnerability to heavy metals in four aquifers using machine learning algorithms, J. Contam. Hydrol. 277 (2026) 104853, http://dx.doi.org/10.1016/j.jconhyd.2026.104853.

[10] F. Noorisafa, A. Razmjou, A. Taheri-Kafrani, F. Ejeian, M. Asadnia, H.A. Ghavamabadi, AI-enhanced smart sensors for heavy metal detection in water treatment, Desalination Water Treat. 325 (2026) 101652, http://dx.doi.org/10.1016/j.dwt.2026.101652.

[11] K. Rezaee, H. Eslami, Bridging machine learning and peptide design for cancer treatment: a comprehensive review, Artif. Intell. Rev. 58 (5) (2025) 156, http://dx.doi.org/10.1007/s10462-025-11148-3.

[12] Z.-W. Gao, Y. Yu, S.-H. Chen, Y.-Y. Li, Z.-H. Liu, M. Yang, P.-H. Li, Z.-Y. Song, X.-J. Huang, Machine learning-driven simultaneous quantification of cd(II) and cu(II) on Co2P/CoP heterostructure: enhanced electrochemical signals via activated Co-P electron bridge, J. Hazard. Mater. 491 (2025) 138030, http://dx.doi.org/10.1016/j.jhazmat.2025.138030.

[13] K. Muthumeenakshi, K. Vijayalakshmi, S. Radha, A machine learning approach for copper detection by halim mediated zinc oxide nanosensor, Nat. Acad. Sci. Lett. (2025) http://dx.doi.org/10.1007/s40009-025-01865-2, URL https://doi.org/10.1007/s40009-025-01865-2.

[14] X. Wang, W. Lin, C. Chen, L. Kong, Z. Huang, D. Kirsanov, A. Legin, H. Wan, P. Wang, Neural networks based fluorescence and electrochemistry dual-modal sensor for sensitive and precise detection of cadmium and lead simultaneously, Sens. Actuators B: Chem. 366 (2022) 131922, http://dx.doi.org/10.1016/j.snb.2022.131922.

[15] Y. Cheng, Z. Xu, Y. Chen, Y. Wang, Z. Lin, J. Liu, A deep learning framework integrating CNN and BiLSTM for financial systemic risk analysis and prediction, in: Proceedings of the 2025 International Conference on Economic Management and Big Data Application, ICEMBDA '25, Association for Computing Machinery, New York, NY, USA, 2025, pp. 270–274, http://dx.doi.org/10.1145/3770177.3770219.

[16] X. Zhu, Q. Ruan, S. Qian, M. Zhang, A hybrid model based on transformer and mamba for enhanced sequence modeling, Sci. Rep. 15 (1) (2025) 11428, http://dx.doi.org/10.1038/s41598-025-87574-8.

[17] R.A. Putri, R. Sarno, W.P. Utomo, F. Taufany, D. Sunaryono, S.I. Sabilla, S.-S. Lee, K.R. Sungkono, T.C. Amri, R.A. Wahyuono, et al., Detecting water contaminants using an electrochemical sensor based on improved transformer encoder with genetic algorithm, J. Water Process. Eng. 87 (2026) 110111, http://dx.doi.org/10.1016/j.jwpe.2026.110111.

[18] B.S. Latibari, H. Homayoun, A. Sasan, Optimizing vision transformers: Unveiling 'focus and forget' for enhanced computational efficiency, IEEE Access 13 (2025) 27908–27927, http://dx.doi.org/10.1109/ACCESS.2025.3540399.

[19] W. Jia, J. Sun, S. Guan, FPQ-itransformer: A novel itransformer-based model for accurate seawater salinity prediction, Environ. Model. Softw. 192 (2025) 106529, http://dx.doi.org/10.1016/j.envsoft.2025.106529.

[20] X. Shen, J. Shen, Y. Zhang, H. Wu, Y. Wang, A multi-source feature engineering-enhanced framework for mid-to-long-term EV charging load forecasting: Integrating self-adaptive optimization and BiLSTM-itransformer predictor, Energy 339 (2025) 139020, http://dx.doi.org/10.1016/j.energy.2025.139020.

[21] A.M. Shiddiqi, A.L. Putra, R.N.E. Anggraini, F.R. Mahhisa, A. Bramantoro, F. Rahma, A.A. Alzahrani, FusionNet-FR: a DualNet transformer architecture using frequency modeling and relational learning for enhanced long-term time series forecasting, PeerJ Comput. Sci. 12 (2026) e3620, http://dx.doi.org/10.7717/peerj-cs.3620.

[22] Y. Han, C. Zeng, Q. Ni, J. Wang, Z. Chu, X. Zhang, Z. Geng, L. Tan, Y. Liu, Time series prediction of anaerobic digestion yield and carbon emissions from food waste based on itransformer model, Chem. Eng. J. 513 (2025) 163064, http://dx.doi.org/10.1016/j.cej.2025.163064.

[23] T. Deng, C. Yang, W. Liu, C. Zhao, R. Li, Y. Huang, TranSpikformer: Enhanced transformer-based spiking neural networks with uniform attention augmentation and depthwise convolutional positional encoding, Knowl.-Based Syst. 336 (2026) 115258, http://dx.doi.org/10.1016/j.knosys.2026.115258.

[24] A.A. Alioghli, F. Yıldırım Okay, Enhancing multivariate time-series anomaly detection with positional encoding mechanisms in transformers: A. Alioghli, f. Okay, J. Supercomput. 81 (1) (2025) 282, http://dx.doi.org/10.1007/s11227-024-06694-6.

[25] M.Y. Ansari, M. Yaqoob, M. Ishaq, E.F. Flushing, I.A.C. Mangalote, S.P. Dakua, O. Aboumarzouk, R. Righetti, M. Qaraqe, A survey of transformers and large language models for ECG diagnosis: advances, challenges, and future directions, Artif. Intell. Rev. 58 (9) (2025) 261, http://dx.doi.org/10.1007/s10462-025-11259-x.

[26] Z. Liu, Z. Fang, Y. Hu, A deep learning-based hybrid method for PM2. 5 prediction in central and western China, Sci. Rep. 15 (1) (2025) 10080, http://dx.doi.org/10.1038/s41598-025-95460-6.

[27] B. Bari, P. Tyagi, U. Udeochu, Cyclic voltammetry insights into Ni/Al-carbonate hydrotalcite catalysis for methanol oxidation, Sci. Rep. 15 (1) (2025) 13365, http://dx.doi.org/10.1038/s41598-025-96933-4.

[28] C.S. Meric, H.A. Deveci, M.M. Kaya, A. Deveci, N. Ozdemir, H. Boyacioglu, M.L. Yola, Determination of paclobutrazol using square wave voltammetry based on a molecularly imprinted polymer and boron-doped copper oxide/graphene nanocomposite, Anal. Methods 17 (2025) 1080–1089, http://dx.doi.org/10.1039/D4AY01947D.

[29] J. Jang, H.-U. Cho, S. Hwang, Y. Kwak, H. Kwon, M.L. Heien, K.E. Bennet, Y. Oh, H. Shin, K.H. Lee, et al., Understanding the different effects of fouling mechanisms on working and reference electrodes in fast-scan cyclic voltammetry for neurotransmitter detection, Analyst 149 (10) (2024) 3008–3016, http://dx.doi.org/10.1039/d3an02205f.

[30] C. Ozdemir, Avg-topk: A new pooling method for convolutional neural networks, Expert Syst. Appl. 223 (2023) 119892, http://dx.doi.org/10.1016/j.eswa.2023.119892.

[31] L. Zhao, Z. Zhang, A improved pooling method for convolutional neural networks, Sci. Rep. 14 (1) (2024) 1589, http://dx.doi.org/10.1038/s41598-024-51258-6.

[32] N. Liu, Y. Zhang, A transformer based visual tracker with restricted token interaction and knowledge distillation, Knowl.-Based Syst. 307 (2025) 112736, http://dx.doi.org/10.1016/j.knosys.2024.112736.

[33] M.H. Rahman, S. Busby, S. Ru, S. Hanif, A. Sanz-Saez, J. Zheng, T.U. Rehman, Transformer-based hyperspectral image analysis for phenotyping drought tolerance in blueberries, Comput. Electron. Agric. 228 (2025) 109684, http://dx.doi.org/10.1016/j.compag.2024.109684.

[34] J.W. Kim, H. Seo, M.J. Kim, J.J. Kim, Quantitative analyses of DPS and PEG-ppg in cu electrolyte using machine learning with artificial neural network, Electrochim. Acta 514 (2025) 145640, http://dx.doi.org/10.1016/j.electacta.2025.145640.

[35] W. Jo, Y. Yoon, M.J. Kim, Machine learning for voltammetric analysis of cu electroplating additives: electrochemically-guided design for dataset structure, J. Electroanal. Chem. 999 (2025) 119552, http://dx.doi.org/10.1016/j.jelechem.2025.119552.
[36] H. Joo, H. Choi, O. Lee, M. Cheon, Bridging KAN and MLP: MJKAN, a hybrid architecture with both efficiency and expressiveness, ICT Express 11 (6) (2025) 1021–1025, http://dx.doi.org/10.1016/j.icte.2025.11.010.
[37] S.-J. Lee, S. young Song, N. rae Lee, M. ju Kim, Y. Ahn, J. Choi, Development and validation of a statistical prediction model for estimating soil lead contamination in a sloped shooting range zone using geochemical and geophysical data, J. Hazard. Mater. Adv. 18 (2025) 100760, http://dx.doi.org/10.1016/j.hazadv.2025.100760.
[38] V.K. Kudapa, S. Chanemougam, S. Ahmad, N.R. Lakkimsetty, Regression models for prediction and evaluation of water contamination, in: Machine Learning in Water Treatment, John Wiley & Sons, Ltd, 2025, pp. 707–718, http://dx.doi.org/10.1002/9781394303526.ch31.
[39] R.A. Putri, R. Sarno, W.P. Utomo, F. Taufany, K.R. Sungkono, T.C. Amri, A. Kamilah, R. Handayani, S.-S. Lee, A.M. Tjoa, A.A. Sagran, Cross-attention feature fusion network for robust estimation of Cd2+ and Pb2+ in water samples using cyclic voltammetry, Chem. Eng. J. Adv. 26 (2026) 101065, http://dx.doi.org/10.1016/j.ceja.2026.101065.
[40] M. Harun-Ur-Rashid, A.B. Imran, T. Foyez, Voltammetric sensors modified with nanomaterials: Applications in rapid detection of bioactive compounds for health and safety monitoring, Discov. Electrochem. 2 (1) (2025) 14, http://dx.doi.org/10.1007/s44373-025-00027-9.
[41] C.S. Ong, Q.H. Ng, A.L. Ahmad, S.C. Low, Enhancement of electrode surface hydrophilicity and selectivity with nafion-PSS composite for trace heavy metal sensing in electrochemical sensors, Anal. Chim. Acta 1335 (2025) 343423, http://dx.doi.org/10.1016/j.aca.2024.343423.
[42] M. Wang, Y. Chen, B. Noureen, Y. Ma, A. Zheng, L. Zhou, M. Liu, Y. Zhao, L. Du, W. Zhang, C. Wu, An electrochemical sensor using nickel-based metal-organic framework towards highly-sensitive detection of multiple heavy metal ions, Sens. Actuators B: Chem. 444 (2025) 138352, http://dx.doi.org/10.1016/j.snb.2025.138352.
[43] Terbium-doped metal-organic frameworks: Dielectric and ferroelectric properties with enhanced electrochemical sensing for heavy metal ion detection, J. Solid State Chem. 341 (2025) 125100, http://dx.doi.org/10.1016/j.jssc.2024.125100.
[44] A. Bank, S. Jafargholinejad, P. Rezai, Lithium detection with microfluidic electrochemical sensor: Proof of concept enhancements by dean flow and lithium manganese oxide, ECS Meet. Abstr. MA2025-01 (59) (2025) 2823, http://dx.doi.org/10.1149/MA2025-01592823mtgabs.
[45] V. Lavanya, K. Santhakumar, A.S. Kumar, Electrocatalytic reduction and sensing of hazardous cr (VI) in water samples using in situ functionalized vanillin-catechol derivative/MWCNT-modified electrode, J. Solid State Electrochem. 29 (1) (2025) 81–94, http://dx.doi.org/10.1007/s10008-024-06096-x.
[46] Z.-X. Huang, Y.-L. Li, J.-C. Peng, T.-T. Ho, H. Huang, M. Aschner, Y.-M. Jiang, The effects of lead, cadmium and arsenic exposure alone or in combination on neurotoxicity through neural signaling pathways, Biol. Trace Elem. Res. (2025) 1–18, http://dx.doi.org/10.1007/s12011-025-04943-0.
[47] V. Kumar, S. Dwivedi, S. Oh, A review on microbial-integrated techniques as promising cleaner option for removal of chromium, cadmium and lead from industrial wastewater, J. Water Process. Eng. 47 (2022) 102727, http://dx.doi.org/10.1016/j.jwpe.2022.102727.
[48] A. Adewumi, O. Ogundele, Hidden hazards in urban soils: A meta-analysis review of global heavy metal contamination (2010–2022), sources and its ecological and health consequences, Sustain. Environ. 10 (1) (2024) 2293239, http://dx.doi.org/10.1080/27658511.2023.2293239.
[49] K. Isinkaralar, Atmospheric deposition of pb and cd in the cedrus atlantica for environmental biomonitoring, Landsc. Ecol. Eng. 18 (3) (2022) 341–350, http://dx.doi.org/10.1007/s11355-022-00503-z.
[50] M. Henry, An ultra-precise fast Fourier transform, Meas.: Sens. 32 (2024) 101039, http://dx.doi.org/10.1016/j.measen.2024.101039.
[51] J.I.Q. Adiba, R. Sarno, K.R. Sungkono, A.T. Haryono, A.M. Tjoa, S.-S. Lee, Wasserstein generative adversarial network with gradient penalty and threshold-enhanced for imbalanced panel data for financial fraud detection, J. Inf. Commun. Technol. 25 (1) (2026) 39–63, http://dx.doi.org/10.32890/jict2026.25.1.3.
[52] D. Aulia, R. Sarno, S.C. Hidayati, M. Rivai, Optimization of the electronic nose sensor array for asthma detection based on genetic algorithm, IEEE Access 11 (2023) 74924–74935, http://dx.doi.org/10.1109/ACCESS.2023.3291451.
[53] M.A. Hasan, R. Sarno, D.R. Wijaya, K.R. Sungkono, S.-S. Lee, N.P. Bimby, A.M. Tjoa, Enhancing long range E-nose based pineapple ripeness classification through odor transfer and wavelet transform, Int. J. Intell. Eng. Syst. 19 (2) (2026) http://dx.doi.org/10.22266/ijies2026.0228.45.
[54] E. Sierra, E. Delenia, A.T. Haryono, R. Sarno, H. Pradana, D. Purwitasari, Clustering-based and multicollinearity feature selection in macroeconomic indicators for predicting loan losses, Int. J. Intell. Eng. Syst. 18 (8) (2025) http://dx.doi.org/10.22266/ijies2025.0930.22.
[55] A. Fajar, R. Sarno, C. Fatichah, R.I. Susilo, G. Pangestu, Cyclical learning rate optimization on deep learning model for brain tumor segmentation, IEEE Access 11 (2023) 119802–119810, http://dx.doi.org/10.1109/ACCESS.2023.3326475.
[56] D. Sunaryono, R. Sarno, S.I. Sabilla, R.A. Putri, T.C. Amri, I. Mirda, J. Siswantoro, Augmented data low confidence (ADLC): A confidence-driven data augmentation framework with ensemble optimization for enhanced machine learning performance, IEEE Access 13 (2025) 201439–201459, http://dx.doi.org/10.1109/ACCESS.2025.3636729.
[57] Q. Li, T. Huang, J. Liu, L. Tan, Time-series vision transformer based on cross space-time attention for fault diagnosis in fused deposition modelling with reconstruction of layer-wise data, J. Manuf. Process. 115 (2024) 240–255, http://dx.doi.org/10.1016/j.jmapro.2024.01.082.
[58] B.J. Kim, H. Choi, H. Jang, D.G. Lee, W. Jeong, S.W. Kim, Improved robustness of vision transformers via prelayernorm in patch embedding, Pattern Recognit. 141 (2023) 109659, http://dx.doi.org/10.1016/j.patcog.2023.109659.
[59] F.E. Keddous, A. Llanza, N. Shvai, A. Nakib, Vision transformers inference acceleration based on adaptive layer normalization, Neurocomputing 610 (2024) 128524, http://dx.doi.org/10.1016/j.neucom.2024.128524.
[60] G. Chanana, Performance analysis of activation functions in molecular property prediction using message passing graph neural networks, Chem. Phys. 591 (2025) 112591, http://dx.doi.org/10.1016/j.chemphys.2024.112591.
[61] A.S. Ali, Z.F. Zaaba, M.M. Singh, M.R.M. Shariff, DropBlock: A structured regularisation technique for mitigating membership inference attacks (MIAs) in machine learning models, ICT Express (2026) http://dx.doi.org/10.1016/j.icte.2026.01.006.
[62] F. Li, C. Xiong, J. He, X. Wang, X. Wang, H. Wu, Application of Self2Self self-supervised denoising framework to airborne gamma-ray spectrometry data, Appl. Radiat. Isot. 230 (2026) 112468, http://dx.doi.org/10.1016/j.apradiso.2026.112468.
[63] Z. Chao, X. Liu, Z. Wu, X. Li, RBF-KAN: Radial basis function-Kolmogorov-Arnold networks, IEEE Internet Things J. (2026) http://dx.doi.org/10.1109/JIOT.2026.3665400, 1–1.
[64] Z. Yang, J. Zhang, X. Luo, X. Wu, Z. Lu, L. Shen, Medkan: An advanced kolmogorov-arnold network for medical image classification, in: 2025 IEEE International Conference on Bioinformatics and Biomedicine, BIBM, IEEE, 2025, pp. 3090–3097, http://dx.doi.org/10.1109/BIBM66473.2025.11356561.
[65] J. Jiang, K.K. Bandeli, K. Srinivasan, Dynamic model selection in enterprise forecasting systems using sequence modeling, Decis. Support Syst. 193 (2025) 114439, http://dx.doi.org/10.1016/j.dss.2025.114439.
[66] L. Tightiz, J. Yoo, W.K. Al-Shibli, Strategic enhancements in electricity price forecasting: The role of XGBoost and error correction features, Results Eng. 26 (2025) 105609, http://dx.doi.org/10.1016/j.rineng.2025.105609.
[67] K. Adhikari, M. Mancini, Z. Libohova, J. Blackstock, E. Winzeler, D.R. Smith, P.R. Owens, S.H. Silva, N. Curi, Heavy metals concentration in soils across the conterminous USA: Spatial prediction, model uncertainty, and influencing factors, Sci. Total Environ. 919 (2024) 170972, http://dx.doi.org/10.1016/j.scitotenv.2024.170972.
[68] J. Piri, M.R.R. Kahkha, O. Kisi, Hybrid machine learning approach integrating GMDH and SVR for heavy metal concentration prediction in dust samples, Environ. Sci. Pollut. Res. 32 (37) (2025) 22082–22101, http://dx.doi.org/10.1007/s11356-024-34795-5.
[69] T. Salazar-Rojas, F.R. Cejudo-Ruiz, G. Calvo-Brenes, Comparison between machine linear regression (MLR) and support vector machine (SVM) as model generators for heavy metal assessment captured in biomonitors and road dust, Environ. Pollut. 314 (2022) 120227, http://dx.doi.org/10.1016/j.envpol.2022.120227.
[70] L. Yu, L. Bai, J. Liu, J. Yang, S. Meng, T. Yang, Y.-H. Yang, R. Hu, Machine learning-assisted fluorescence/smartphone dual-mode platform for lead ion detection using the novel polyimide covalent organic framework, Talanta 295 (2025) 128346, http://dx.doi.org/10.1016/j.talanta.2025.128346.